Available online at www.sciencedirect.com
ScienceDirect
Comput. Methods Appl. Mech. Engrg. 283 (2015) 1382–1400
Computer methods in applied mechanics and engineering
www.elsevier.com/locate/cma

A NURBS-based interface-enriched generalized finite element scheme for the thermal analysis and design of microvascular composites

Marcus H.Y. Tan[a], Masoud Safdari[b], Ahmad R. Najafi[a], Philippe H. Geubelle[b,*]

[a] *Department of Mechanical Science and Engineering, University of Illinois, Urbana, IL 61801, USA*
[b] *Department of Aerospace Engineering, University of Illinois, Urbana, IL 61801, USA*

Received 16 February 2014; received in revised form 8 September 2014; accepted 9 September 2014
Available online 21 September 2014

Highlights

- We develop a NURBS-based interface-enriched generalized finite element method.
- We use the method to solve a simplified thermal model of a network of micro-channels in composites.
- Solutions significantly more accurate than standard FEM are obtained with coarse meshes.
- Near-optimal convergence rate is obtained.
- Geometry of curved micro-channels can be handled exactly.

Abstract

Motivated by recent advances in manufacturing techniques for high-temperature microvascular composites, a NURBS-based interface-enriched generalized finite element method (IGFEM) is developed to solve a simplified thermal model of microchannels embedded in the materials. This method is capable of handling curved and branched microchannels. Solutions more accurate than those achieved with the conventional finite element method can be obtained with coarse meshes that do not conform to the geometry of the microchannels. Near-optimal asymptotic convergence rate is also achieved with this method even for highly curved microchannels. The capability of the numerical scheme is demonstrated by solving problems with complex microchannel configurations.
© 2014 Elsevier B.V. All rights reserved.

Keywords: NURBS; Interface-enriched generalized finite element method; Microvascular composites; Thermal; Curved microchannel; Microchannel network

1. Introduction

Microvascular materials are a class of biologically-inspired materials that mimic the vascular systems found in nature. The recent development of a manufacturing technique for microvascular composites based on a sacrificial

* Corresponding author. Tel.: +1 217 2447648; fax: +1 217 2440720.
E-mail addresses: geubelle@uiuc.edu, geubelle@illinois.edu (P.H. Geubelle).

http://dx.doi.org/10.1016/j.cma.2014.09.008
0045-7825/© 2014 Elsevier B.V. All rights reserved.

fiber approach has enabled the creation of complex networks of microchannels embedded in composite parts [1]. By changing the fluid flowing in the microchannels, the material is capable of multifunctional applications such as thermal management, manipulation of electromagnetic signature, electrical conductivity tuning and chemical reactivity [1–3]. In many of these applications (thermal, structural, electromagnetic), the presence of the microchannels results in fields with discontinuous gradients in the material. Hence, the computational analysis and design of microvascular composites require a method capable of capturing weakly discontinuous solution fields, i.e., solutions that are C^0-continuous with finite gradient jumps.

Standard finite element methods (SFEM) can be applied to solve such problems provided a mesh that conforms to the geometry of the microchannels is used. Solutions obtained with non-conforming meshes have poor accuracy as the error bound of the a priori error estimate shows that a weakly discontinuous solution field converges suboptimally. With a conforming mesh, the C^0 continuity of the FEM solution across the element boundaries naturally captures the discontinuity of the gradient fields and optimal convergence can be recovered. However, generating a conforming mesh with good quality elements can be a challenging process especially for complex networks of embedded microchannels. For transient [4] or optimization [5,6] problems, reconstructing a conforming mesh at each iteration can be a formidable and inefficient process, and might violate energy conservation [7].

The generalized FEM (GFEM) [8] and extended FEM (XFEM) [9] are widely-used and successful methods to handle weakly or strongly discontinuous fields with non-conforming meshes. These methods are based on the partition of unity method in which enrichment functions that closely approximate the true solution are multiplied by the partition of unity functions to construct the local enrichment functions [10–12]. The GFEM and XFEM have been developed to handle strongly discontinuous problems such as crack propagation [7,9,13] and weakly discontinuous problems such as material interface [14] and intense thermal loading due to shockwave [4]. Closely related to this work is a GFEM developed to capture weakly discontinuous temperature field in the thermal analysis, design and optimization of microvascular materials [5,6,15].

Recently, an interface-enriched generalized FEM (IGFEM) that has some advantages over GFEM/XFEM has been proposed [16,17]. In the method, enrichment nodes are introduced at the intersections between the non-conforming elements and the interface, and associated with them are the enrichment functions. This approach allows local enrichment functions to be constructed without using partition of unity functions. The advantages of this method over GFEM/XFEM are straightforward application of essential boundary conditions and a lower number of degrees of freedom. However, interfaces are still approximated as line segments in the original IGFEM method.

The aforementioned improvement in manufacturing techniques has allowed the creation of microvascular materials with complex curved microchannels [1,18]. In this regard, an XFEM that has been developed for curved strong and weak discontinuities [19] could potentially be applied in the analysis of microvascular composites. The approach summarized in [19] describes the interface by a level set function, which is then approximated by standard finite element interpolation.

In the present study, we adopt a different approach and develop a non-uniform rational B-spline (NURBS)-based IGFEM for triangular linear elements to handle curved microchannels described by NURBS. NURBS include B-splines as a special case. Among the many advantages of using NURBS are their ability to model complicated geometry with high accuracy, the abundance of algorithms and methods for manipulating NURBS, as well as being the standard of Computer Aided Design (CAD) [20,21]. The use of NURBS enrichment functions is inspired by a series of methods that incorporate NURBS in FEM, including isogeometric analysis [22]. Isogeometric analysis provides a seamless integration with CAD by using NURBS for both the geometrical description of the domain and the construction of the basis functions of the finite element solution. To handle complex geometries, the domain has to be decomposed into patches that conform to the curved boundaries. In addition, one must ensure that the mapping and parameterization in adjoining patch faces are identical in the coarsest mesh and subsequent mesh refinement must also ensure continuity of the solution between the patches [23]. This may be very challenging in the presence of patches with complex geometry. To overcome these issues, NURBS-enhanced FEM (NEFEM) has been proposed to handle curved boundaries [24]. In that method, curved triangular elements are constructed along curved boundaries and handled with NEFEM while other elements are treated with SFEM. Exact geometrical mapping from a reference element to a curved triangular element is defined using the NURBS description of the curved boundaries. Consistency in the approximation is also ensured by using Cartesian shape functions, i.e., the degree of polynomial interpolation in physical space is the same as the degree of the shape functions. Hence the NEFEM overcomes the geometric inaccuracy

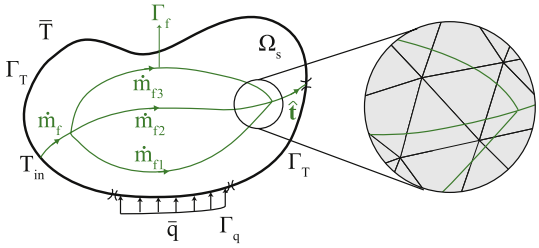

Fig. 1. Schematic of the geometry and boundary conditions of the model problem. The domain consists of a solid Ω_s and microchannels Γ_f. The mass flow rates in the microchannels satisfy mass conservation, i.e., $\dot{m}_f = \dot{m}_{f1} + \dot{m}_{f2} + \dot{m}_{f3}$. The direction of the flow at each point of Γ_f is specified by the unit tangent vector $\hat{\mathbf{t}}$. The inlet temperature T_{in} is prescribed. The inset schematically shows a portion of an unstructured non-conforming mesh.

in Cartesian FEM and the lack of consistency in p-FEM [24]. However, the method still requires the generation of a mesh that conforms to the geometry of the curved boundary.

NURBS-based XFEM's have also been proposed to represent curved integration subdomains exactly by NURBS [25,26]. For example, the approach described in [25] represents the integration subdomains with NURBS surfaces. The interfaces are described by level set functions, which are then discretized and approximated by NURBS curves to generate the NURBS surfaces. In addition, this method requires the use of quadratic or higher-order shape functions as linear shape functions cannot ensure the continuity of the displacement field across the interface of deformed elements.

In contrast to NEFEM and the methods described in [19,25], the NURBS-based IGFEM proposed hereafter uses linear shape functions associated with the original nodes of a non-conforming triangular element and places the enrichment nodes strategically on or near the curved interface, thus reducing the number of new degrees of freedom. Similar to [25], the integration subdomains are represented by NURBS surfaces. However, unlike [19,25], we use NURBS enrichment functions instead of enrichment functions based on the level set functions. Therefore, NURBS representation of a curved interface can be used at the outset, obviating the need for approximation of the curved interface. Similar to isogeometrical analysis, the key advantage of using NURBS is that the microchannel geometry can be imported from and exported to CAD programs without loss of geometrical information.

The paper is organized as follows. In Section 2, we describe the problem of interest, i.e., the heat equation with a line source/sink. In Section 3, we show how NURBS enrichment functions are constructed. We then perform in Section 4 a detailed convergence study using the method of manufactured solution for semicircular microchannels and for branching microchannels. Finally, we apply the NURBS-based IGFEM in Section 5 to solve heat transfer problems in actively-cooled microvascular materials with various microchannel geometries.

2. Problem description

A microvascular material is represented by a domain Ω embedded with microchannels Γ_f modeled as line source or sinks as shown in Fig. 1. This simplification is possible because the microchannel diameters are typically much smaller than the distance between them and other characteristic dimensions of the problem. Let T, $\dot{m}_f$, c_f and s respectively denote the temperature field, the mass flow rate and specific heat capacity of the fluid, and the parametric coordinate along the microchannel in the flow direction. A simple energy balance over a small portion of a microchannel yields the following expression for the heat flow rate per unit length of the microchannel [27]

$$q = \dot{m}_f c_f \frac{dT}{ds}. \tag{1}$$

This equation assumes that the flow is fully developed, that thermal conduction along the microchannel is negligible, and that the mixed-mean temperature of the fluid (defined as the average temperature in a cross section weighted by the volumetric flow rate in that cross-section [27]) is approximately the wall temperature. It also assumes that the thermal diffusivity is large enough, the flow rate and the temperature gradient along the channel are not too large, and the ratio of the diameter to length of the channel is small.

Let the boundary of Ω be divided into 2 parts Γ_T and Γ_q where the Dirichlet and Neumann boundary conditions are specified, respectively. Given the thermal conductivity tensor $\boldsymbol{\kappa}$ of the solid Ω_s, the unit tangential vector field $\hat{\mathbf{t}}$

indicating the direction of flow in Γ_f, and the distributed heat source f, the weak formulation of the problem is: find the temperature field T satisfying the Dirichlet boundary condition $T_{|\Gamma_T} = \bar{T}$ such that

$$a(v, T) = (v, f) + (v, \bar{q})_{\Gamma_q} \quad \forall v \in V, \tag{2}$$

where

$$\begin{aligned} a(v, T) &= \int_{\Omega_s} \nabla v \cdot (\boldsymbol{\kappa} \nabla T)\, \mathrm{d}\Omega + \int_{\Gamma_f} v c_f \dot{m}_f \mathbf{t} \cdot \nabla T\, \mathrm{d}\Gamma, \\ (v, f) &= \int_{\Omega_s} v f\, \mathrm{d}\Omega, \\ (v, \bar{q})_{\Gamma_q} &= \int_{\Gamma_q} v \bar{q}\, \mathrm{d}\Gamma, \end{aligned} \tag{3}$$

and V is the space of weighting functions and $\bar{q}$ is the prescribed heat flux. Note that the presence of the convective term in (2) implies that the associated stiffness matrix is not symmetric. Unlike the convective term obtained by modeling the microchannels with non-zero thickness [16], this term only causes instability in the form of numerical oscillations at very high flow rates, well beyond the regime of interest. Hence, no numerical stabilization such as SUPG [28] is needed to stabilize the solution.

3. NURBS-based IGFEM formulation

Let there be n original nodes in the non-conforming mesh. Let the nodal value T_i and the Lagrangian shape function $N_i(\mathbf{x})$ be associated with a node i. In the IGFEM formulation [16], n_{en} enrichment nodes are added along the interface to yield the following expression for the finite element solution:

$$T^h(\mathbf{x}) = \sum_{i=1}^{n} T_i N_i(\mathbf{x}) + \sum_{j=1}^{n_{\text{en}}} \beta_j \psi_j(\mathbf{x}), \tag{4}$$

where ψ_j is the enrichment function associated with enrichment node j and β_j is the generalized degree of freedom. Instead of the linear polynomial enrichment functions adopted in [16], we use in this work NURBS enrichment functions, the construction of which is explained in the remainder of this section. We begin by briefly introducing NURBS curves and surfaces, covering only the needed concepts and terminologies. The reader is referred to [20,21,23] for a detailed explanation of NURBS relevant to this work.

A NURBS curve is defined by

$$\mathbf{C}(\xi) = \sum_{i=1}^{n} \mathbf{B_i} R_i^p(\xi), \tag{5}$$

where $\mathbf{B_i}$ is the ith control point and R_i^p is the degree p rational B-spline basis function associated with the control point. The basis functions R_i^p are defined as

$$R_i^p(\xi) = \frac{N_i^p(\xi) w_i}{\sum_{j=1}^{n} N_j^p(\xi) w_j}, \tag{6}$$

where N_i^p are B-spline basis functions, which can be generated by a recursion formula [20,21,23]. The shape of the curve can be changed by adjusting the location of the control points and the weights w_i, thus allowing the exact representation of complex geometries that cannot be represented by B-spline curves such as conics. Moreover, the geometry is also controlled by a set of $n + p + 1$ coordinates/knots/break points in parametric space called the knot vector $\boldsymbol{\xi} = \{\xi_1, \xi_2, \ldots, \xi_{n+p+1}\}$. The knot vector determines the form, support and smoothness of N_i^p. The curve is only defined on the interval $\xi \in [\xi_1, \xi_{n+p+1}]$. In this work, only open knot vectors, which are standard in CAD [21], are considered. In an open knot vector, the first and last knots appear $p + 1$ times.

A NURBS surface is defined analogously by

$$\mathbf{S}(\xi,\eta)=\sum_{i=1}^{n}\sum_{j=1}^{m}\mathbf{B_{ij}}R_{i,j}^{p,q}(\xi,\eta), \tag{7}$$

where

$$R_{i,j}^{p,q}(\xi,\eta)=\frac{N_i^p(\xi)M_j^q(\eta)w_{i,j}}{\sum_k^n\sum_l^m N_k^p(\xi)M_l^q(\eta)w_{k,l}}. \tag{8}$$

The set of control points $\{\mathbf{B_{ij}}\}$ is called the control net and associated with each control point is a weight $w_{i,j}$. The rational basis functions $R_{i,j}^{p,q}$ consist of tensor products of 1D B-spline basis functions $N_i^p(\xi)$ and $M_j^q(\eta)$. Instead of a single knot vector, two knot vectors $\boldsymbol{\xi}=\{\xi_1,\xi_2,\ldots,\xi_{n+p+1}\}$ and $\boldsymbol{\eta}=\{\eta_1,\eta_2,\ldots,\eta_{m+q+1}\}$ are needed to define the surface, which is only defined in $[\xi_1,\xi_{n+p+1}]\times[\eta_1,\eta_{m+q+1}]$.

The construction of the NURBS enrichment function consists of four steps:

1. Finding the intersections between the microchannels and the non-conforming elements.
2. Extracting the NURBS representation of a segment of a microchannel in an element.
3. Constructing the NURBS representation of the integration subdomains of a parent element, defined as an element cut by a microchannel.
4. Using some of the rational basis functions of the NURBS representation of the integration subdomains as enrichment functions.

These four steps are summarized next, followed by a description of the integration scheme.

3.1. Intersection between the microchannels and the elements

In this work, the non-conforming meshes are made of triangular elements. Due to the many different ways in which a curved microchannel can intersect an element, we restrict our work to cases in which each edge of an element intersects with each microchannel at most once. When this condition is not satisfied, it is an indication that the curvature of the microchannel is likely too high in the region containing the element. In this case, local mesh adaptation such as mesh refinement, mesh reconnection and mesh movement [29] can be carried out until the condition is satisfied. We also assume that at most one branch point appears on the boundary or the interior of an element.

The intersection between the edge of an element and a curved microchannel is found by using a non-linear solver. The search direction is found by the Levenberg–Marquardt algorithm [30]. To drastically reduce the number of iterations required to find the solution as well as ensuring that the non-linear solver does not miss the solution due to a poor initial guess, the curved microchannel is discretized into a series of linear segments to obtain an initial guess close to the true solution (if it exists). The end point of a linear segment closest to the edge is taken as the initial guess. To prevent unnecessary work in finding the intersections when they do not exist, a convex hull tightly containing the NURBS curve and determined by the control points of the NURBS curve can be used [20]. An edge that lies outside the convex hull is immediately excluded from consideration.

3.2. Extraction of NURBS curve segment

Suppose a NURBS curve of degree p with knot vector $\boldsymbol{\xi}=\{\xi_1,\xi_2,\ldots,\xi_{n+p+1}\}$ intersects an element at $\xi=a\in(\xi_k,\xi_{k+1}]$ and $\xi=b\in(\xi_l,\xi_{l+1}]$ with $b>a$. Using Fig. 2 as illustration, the NURBS curve is defined by the control points $\mathbf{B}_1,\ldots\mathbf{B}_4$ and the knot vector $\boldsymbol{\xi}=\{0,0,0,0.5,1,1,1\}$. Let us also assume in this illustrative example that the intersections with the element occur at $\xi=0.39$ and 0.65 on the NURBS curve. The curve segment can be extracted in the following manner:

1. Insert knots at $\xi=a$ and $\xi=b$ using a knot insertion algorithm described in [21,22] until there are $p+1$ knots at $\xi=a$ and $\xi=b$ in the resulting knot vector. The knot insertion algorithm adds a control point with every knot insertion and the resulting curve is exactly the same as the original curve with the same smoothness as before. After the multiple knot insertions, the resulting knot vector is $\boldsymbol{\xi}'=\{0,0,0,0.39,0.39,0.39,0.5,0.65,0.65,0.65,1,1,1\}$

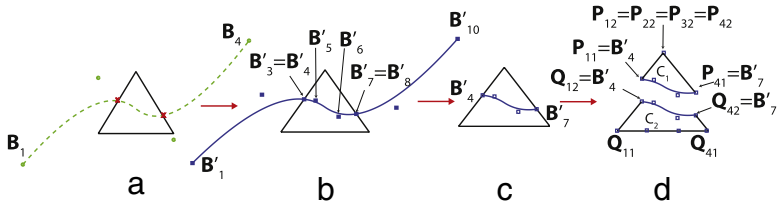

Fig. 2. Extraction of a NURBS curve segment and construction of integration subdomains. When there is no branching in the interior of the element, (a) find intersections of a curve with the element edges, (b) perform knot insertions, (c) extract the curve segment and (d) construct the integration subdomains.

and there will be two coincident control points $\mathbf{B}'_3, \mathbf{B}'_4$ exactly at the intersection corresponding to $\xi = a$ and two other coincident control points $\mathbf{B}'_7, \mathbf{B}'_8$ at $\xi = b$. Let $i_{\min} = \min(i)$ such that $\xi'_i \geq a$ and $i_{\max} = \max(i)$ such that $\xi'_i \leq b$. In general the pairs of coincident control points are $\mathbf{B}'_{i_{\min}-1}, \mathbf{B}'_{i_{\min}}$ and $\mathbf{B}'_{i_{\max}-p-1}, \mathbf{B}'_{i_{\max}-p}$.

2. The curve segment within the element can then be represented exactly by the control points $\mathbf{B}'_4$ to $\mathbf{B}'_7$ and the knot vector $\overline{\boldsymbol{\xi}} = \{0.39, 0.39, 0.39, 0.5, 0.65, 0.65, 0.65\}$. In general, the control points of the extracted curve segment are $\mathbf{B}'_i, i = i_{\min}, \ldots, i_{\max} - p - 1$ and the knot vector is $\overline{\boldsymbol{\xi}} = \{\xi'_{i_{\min}}, \ldots, \xi'_{i_{\max}}\}$.

Note that the weights can be extracted in exactly the same fashion as the control points.

3.3. Construction of NURBS representation of an integration subdomain

Two general cases need to be handled given the restriction that each edge of an element has at most one intersection with a microchannel. The first case occurs when there is no branching in the parent element as shown in Fig. 2. To construct the NURBS enrichment function, we need the NURBS representations of the integration subdomains shown in Fig. 2(d). The NURBS representation of the triangular integration subdomain (C_1) is given by

$$\mathbf{S}_{C_1}(\xi, \eta) = \sum_{i=1}^{n} \sum_{j=1}^{2} \mathbf{P_{ij}} \overline{R}^{p,1}_{i,j}(\xi, \eta), \tag{9}$$

with $n = 4$, $p = 2$, $\mathbf{P}_{11} = \mathbf{B}'_4$, $\mathbf{P}_{21} = \mathbf{B}'_5$, $\mathbf{P}_{31} = \mathbf{B}'_6$, $\mathbf{P}_{41} = \mathbf{B}'_7$ and the other control points coinciding with the apex of C_1. The NURBS representation of the quadrilateral integration subdomain (C_2) is given by

$$\mathbf{S}_{C_2}(\xi, \eta) = \sum_{i=1}^{n} \sum_{j=1}^{2} \mathbf{Q_{ij}} \tilde{R}^{p,1}_{i,j}(\xi, \eta), \tag{10}$$

with $n = 4$, $p = 2$, $\mathbf{Q}_{12} = \mathbf{B}'_4$, $\mathbf{Q}_{22} = \mathbf{B}'_5$, $\mathbf{Q}_{32} = \mathbf{B}'_6$, $\mathbf{Q}_{42} = \mathbf{B}'_7$ and the other control points are equally spaced along the bottom edge. For both (9) and (10), the knot vector $\overline{\boldsymbol{\xi}}$ is the knot vector of the extracted curve segment, i.e., $\overline{\boldsymbol{\xi}} = \{0.39, 0.39, 0.39, 0.5, 0.65, 0.65, 0.65\}$ in this example and the other knot vector is $\overline{\boldsymbol{\eta}} = \{0, 0, 1, 1\}$. It is worth noting that as long as each microchannel does not intersect an element edge more than once, the method described here can be extended readily to the case of multiple microchannels in an element by splitting the parent element into more than two integration subdomains with some of the integration subdomains having more than one curved boundaries.

The second case involves a branching point in the interior of the non-conforming element as shown in Fig. 3. As before, the intersection points are determined and the curves are extracted. The quadrilateral integration subdomains C_3 and C_4 as shown in Fig. 3(b) have to be further triangulated to produce enrichment functions that have inter-element continuity. Details on the definition of the enrichment functions and the integration scheme for this case are provided in the next section.

3.4. Construction of NURBS enrichment functions

The central idea of the construction of NURBS enrichment functions is to use the control points describing the microchannel edge of the integration subdomains as enrichment nodes and the basis functions associated with these control points as enrichment nodes in the same spirit as the original IGFEM. The choice of these basis functions as

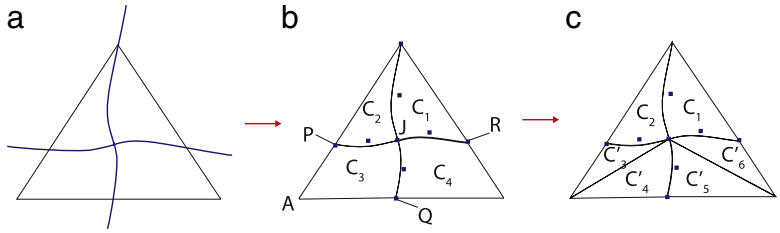

Fig. 3. When there is branching in the interior of the element, (a) intersections are determined, (b) curve segments are extracted, (c) quadrilateral subdomains are triangulated.

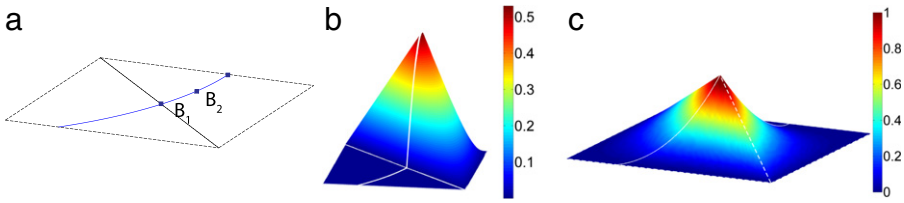

Fig. 4. (a) A pair of triangular elements cut by a circular arc. (b) and (c): The enrichment functions for enrichment nodes B_2 and B_1, respectively.

enrichment functions is straightforward and is motivated by the fact that the enrichment functions have C^0 continuity across the integration subdomains and across the elements as we will explain later. Moreover, the discontinuous gradient in an enrichment function occurs exactly on the channel. We again refer to the example in Fig. 2 for illustration. Enrichment nodes are introduced at the control points along the microchannel, i.e., at $\mathbf{B}'_4, \ldots, \mathbf{B}'_7$. The enrichment functions associated with these nodes are $\overline{R}^{2,1}_{1,1}$, $\overline{R}^{2,1}_{2,1}$, $\overline{R}^{2,1}_{3,1}$ and $\overline{R}^{2,1}_{4,1}$ in C_1 and $\tilde{R}^{2,1}_{1,2}$, $\tilde{R}^{2,1}_{2,2}$, $\tilde{R}^{2,1}_{3,2}$ and $\tilde{R}^{2,1}_{4,2}$ in C_2.

The enrichment function associated with an interior enrichment node such as $\mathbf{B}'_5$ in Fig. 2 or $\mathbf{B_2}$ in Fig. 4(a) is continuous across the integration subdomains because the subdomains share the same curve segment used to construct their NURBS surfaces. It is also continuous across the elements simply because it vanishes at the edges of the element as shown in Fig. 4(b). That the enrichment function associated with an exterior enrichment node is continuous across elements can be explained by an example. Consider the enrichment node $\mathbf{B}'_4$ in Fig. 2. The basis functions associated with $\mathbf{B}'_4$ of the NURBS surfaces C_1 and C_2 vary linearly along the edges $\mathbf{P}_{12}\mathbf{B}'_4$ and $\mathbf{Q}_{11}\mathbf{B}'_4$, respectively, are unity at $\mathbf{B}'_4$ and vanish along the other edges of the element. Similarly, the basis functions of the integration subdomains in the element adjacent to the edge $\mathbf{P}_{12}\mathbf{Q}_{11}$ have the same property by construction. The same argument applies to enrichment node $\mathbf{B_1}$ in Fig. 4(a). Hence these enrichment functions also have inter-element continuity, which can clearly be observed in Fig. 4(c).

The construction of enrichment function for an element with a branching point is the same as before, except that care must be taken to ensure that the enrichment function is continuous between elements. If two adjacent edges of a quadrilateral integration subdomain are described by curve segments with more than 2 control points, the enrichment function constructed in this manner is not continuous across the element. For illustration, consider integration subdomain C_3 of Fig. 3(b), the basis functions associated with P are non-linear along the straight edge PA. However, the basis function associated with P of the NURBS surface describing the adjacent integration subdomain in the neighbor element is linear along PA. Hence the enrichment function is discontinuous. To prevent this problem, the quadrilateral integration subdomain has to be further subdivided as shown in Fig. 3(c). The basis function associated with P of integration subdomain C'_3 is then a linear function along edge PA and inter-element continuity is ensured.

3.5. Integration over a parent element

Work on the optimal quadrature rule for NURBS is still an active area of research [31]. It is known that Gaussian quadrature is not an optimal rule as it does not utilize the smoothness of the NURBS function between knot spans [31]. An optimal rule called the "half-point rule", which corresponds to one integration point every two basis functions regardless of degree has been developed for the exact integration of B-splines in 1D [31]. The half-point rule will

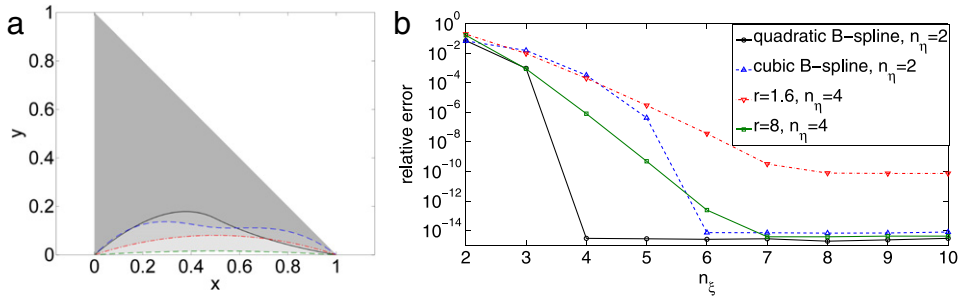

Fig. 5. (a) A triangular domain with one curved edge for the numerical integration study. (b) The relative error of the numerical integration of (12) using Gaussian quadrature.

result in huge savings in isogeometric analysis because NURBS quadrature is carried out everywhere in the domain. In our case, we only need to perform quadrature of NURBS in enriched elements and hence an optimal rule is not critical to our method. Because the "half-point rule" has not been tested on piecewise rational polynomials and for simplicity, we use Gaussian quadrature.

Similar to the original IGFEM [16], integration is performed separately in each integration subdomain. However, when using a NURBS enrichment function, two Jacobians are needed [23]. The geometrical mapping from the physical space to the NURBS parametric space in (9) or (10) is used to calculate the first Jacobian. The derivative of rational B-splines can be calculated according to the method described in [20]. A linear mapping from a knot span to the usual local coordinate space should be defined so that Gaussian quadrature can be performed. This mapping gives rise to the second Jacobian.

Given a knot vector $\boldsymbol{\xi} = \{\xi_1, \xi_2, \ldots, \xi_{n+p+1}\}$, the knot spans are the sub-intervals $[\xi_i, \xi_{i+1}]$. The Gaussian quadrature is applied separately in each knot span with non-zero width. For example, if the integration subdomain is described by a NURBS with knot vectors $\boldsymbol{\xi} = \{0, 0, 0, 0.5, 1, 1, 1\}$ and $\boldsymbol{\eta} = \{0, 0, 1, 1\}$ and the number of Gauss points per knot span in the ξ- and η-directions are n_ξ and n_η, respectively, then the total number of Gauss points is $2n_\xi \times n_\eta$. The number of Gauss points per knot span depends on the degree of the NURBS surface in the direction of the knot vector. In general the higher the degree, the higher the number of Gauss points per knot span. In this subsection, we perform a simple study on the number of Gauss points required for integration specific to our work. The appropriate selection of quadrature rule in the general case warrants a separate study on its own.

Consider a triangular integration subdomain as shown in Fig. 5(a) with one curved edge. Consider a typical term in our element stiffness matrix given by

$$\iint_{[0,1]^2} \nabla_{\mathbf{x}}^T \psi_i(\xi, \eta) \nabla_{\mathbf{x}} \psi_j(\xi, \eta) J(\xi, \eta) \mathrm{d}\xi \mathrm{d}\eta, \tag{11}$$

where ψ_i, ψ_j are enrichment functions and $J(\xi, \eta)$ is the determinant of the Jacobian from the physical space to the NURBS parameter space. A common practice when integrating such a term in isogeometric analysis is to assume that the Jacobian is a constant and if ψ_i and ψ_j are rational piecewise polynomials, that the denominator varies slowly compared to the numerator that it can be assumed constant. This practice is based on standard FEM, where the integration order required is deduced by assuming an undistorted element.

However, in our study, we do not assume that the Jacobian is constant. Because the derivative of a NURBS basis function with respect to physical space in a curved integration subdomain results in an unknown function type, we assume that the derivative has the same degree as the basis function itself. Note that this has also been done for isogeometric analysis when determining an appropriate integration order for the stiffness matrix [31]. Hence in lieu of the term in (11), we perform an integration study over a triangular integration subdomain with a curved edge represented by NURBS as shown in Fig. 5(a) on a term given by

$$\iint_{[0,1]^2} \psi(\xi, \eta)^2 J(\xi, \eta) \mathrm{d}\xi \mathrm{d}\eta, \tag{12}$$

where ψ is chosen as one of the enrichment functions associated with the interior enrichment nodes. The curved edge is a quadratic B-spline, a cubic B-spline and two rational NURBS circular arcs of different radii. The control points

of the curves can be found in Table A.1 of Appendix. The different radii are chosen based on the radius to mesh size ratios of the semicircular channel problem in Section 4.1.

Fig. 5(b) shows how the relative error changes with respect to the number of Gauss points in the direction ξ, n_ξ while fixing n_η. ξ and η are chosen to be in the directions of the curved and straight edges, respectively. Because the basis function in η for the B-splines is a linear piecewise polynomial, $n_\eta = 2$ is the necessary minimal number of Gauss points required to integrate (12) exactly. Fig. 5(b) shows that $n_\xi = 4$ and 6 are required to integrate the quadratic and cubic B-splines, respectively. This is expected because the integrand in (12) has degrees 6 and 10 for quadratic and cubic B-splines, respectively.

On the other hand, the quadrature rule for a rational NURBS is not straightforward. We base our selection of number of quadrature points on the finite element solution error in Section 4.1. For the NURBS curves, $n_\eta = 4$ is chosen because $n_\eta = 2$ or 3 will limit the relative error of the integration to between 10^{-2} and 10^{-3}, which may be insufficient when the radius of curvature is high. Fig. 5(b) shows that the relative error at $n_\xi = 4$ for the smaller radius of $r = 1.6$ is slightly greater than 10^{-4}, which is smaller than the finite element solution error presented in Section 4.1. As the mesh size becomes smaller, the ratio of the radius to the mesh size becomes larger and the relative error of the quadrature decreases. For the larger radius of $r = 8$ and at $n_\xi = 4$, the relative error decreases to a value slightly greater than 10^{-6}, which is much smaller than the finite element solution error. Therefore, we recommend a $n_\xi = n_\eta = 4$ quadrature rule for a radius to mesh size ratio greater than 1.6. The numerical integration study here is also valid for a quadrilateral element with one curved edge.

Other than the usual first term in the stiffness matrix of (2), a second term arises due to the contribution of the microchannels. In an integration subdomain, this integration is only performed over the edge of the subdomain coinciding with a microchannel. Since there are two integration subdomains sharing a microchannel, the contribution of this integral is halved for each subdomain to avoid double counting.

3.6. Computational cost

The creation of meshes that conform to complex microstructural details such as material interfaces and embedded microchannels often represents a challenging and time-consuming task. This is especially the case in 3D settings and/or for problems that require the simulation of multiple realizations of the virtual microstructure such as in multiscale modeling (for which multiple realizations are needed to extract some of the statistics of the homogenized response) or mesoscale shape optimization (during which multiple simulations of the evolving microstructure have to be performed). The ability to perform multiple simulations with a single non-conforming mesh, thereby avoiding the complexity and cost of meshing, is undoubtedly one of the attractive features of the NURBS-based IGFEM scheme. Although it often represents the major time consuming part of a finite element analysis, the mesh generation process does not usually enter the assessment of the efficiency of a solution method. It is therefore difficult to perform a direct comparison between the NURBS-based IGFEM and the standard FEM.

As far as the solution step itself, the key computational costs involved with the IGFEM are associated with (i) finding the intersection points, (ii) constructing the enrichment functions, (iii) assembling the stiffness matrix and (iv) solving the system of equations. With regard to the first operation, efficient algorithms to find the intersection of NURBS with element edges and faces, such as implicitization, subdivision and Bézier clipping, are widely available [32–35]. Furthermore, finding the intersection points and constructing the enrichment functions can be readily parallelized. While the numerical integration associated with the computation of the stiffness matrix in the IGFEM is more expensive than its standard FEM counterpart, this step can be further improved as the Gaussian quadrature rule for integration of NURBS is not optimal because it does not utilize the smoothness of the curve between knot spans [31]. It should be noted that, unlike isogeometric analysis, NURBS-based IGFEM only requires integration of NURBS in the enriched elements, which typically represent a relatively small fraction of the entire mesh. In most large size problems, the solution of the resulting system of equations constitutes by far the most time-intensive part of the analysis.

4. Convergence study

We use the method of manufactured solutions for a problem with a curved microchannel without branching and a second problem with straight branched microchannels to study the convergence and accuracy of IGFEM with NURBS

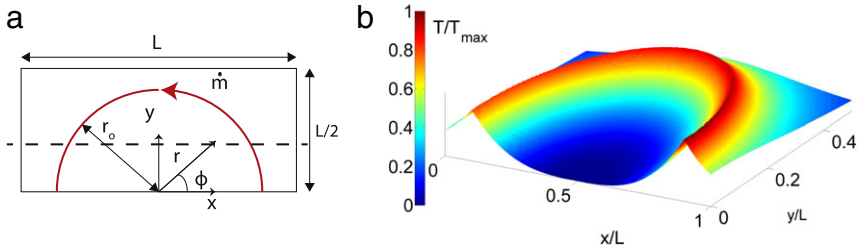

Fig. 6. (a) Domain geometry for Verification Problem 1. (b) 3D surface plot of the analytical solution for $k = 3$, $\alpha = 90$ and $r_o = 0.4$. The temperature has been normalized by the maximum temperature in the domain, $T_{\max}$.

enrichment functions. Dirichlet boundary conditions are imposed at the boundary using the manufactured solutions. The study is carried out using the L^2- and H^1-norms of the error defined as

$$\|T - T^h\|_{L^2(\Omega)} = \sqrt{\int_\Omega (T - T^h)^2 \mathrm{d}\Omega}, \tag{13}$$

and

$$\|T - T^h\|_{H^1(\Omega)} = \sqrt{\int_\Omega \Big[(T - T^h)^2 + \big(\|\nabla T - \nabla T^h\|_2\big)^2\Big] \mathrm{d}\Omega}. \tag{14}$$

We also study the effect of curvature on the relative error of the solution. The problems in the remaining sections involve a homogeneous solid of uniform thermal conductivity κ, with the weak discontinuity in the temperature field solely due to the presence of the microchannels.

4.1. Verification Problem 1: semicircular channel

Consider a semicircular channel of radius r_o centered at $(L/2, 0)$ with mass flow rate $\dot{m}_f$ and uniform heat capacity c_f in a rectangular domain of length L and width $L/2$ as shown in Fig. 6(a). The semicircle can be described by the control points $(L/2 + r_o, 0)$, $(L/2 + r_o, r_o)$, $(L/2, r_o)$, $(L/2 - r_o, r_o)$, $(L/2 - r_o, 0)$ with corresponding weights $1, 1/\sqrt{2}, 1, 1/\sqrt{2}, 1$ and knot vector $\{0, 0, 0, 1, 1, 2, 2, 2\}$. By choosing a characteristic temperature ($T_{\max}$) and a characteristic length (L), the weak form (2) can be expressed in terms of a single dimensionless parameter given by

$$\alpha = \frac{\dot{m} c_f}{\kappa}. \tag{15}$$

If the following distributed heat source is applied to Ω_s:

$$f(r, \phi) = \begin{cases} -(k^2 + \lambda^2) r_o^2 \left(\dfrac{r}{r_o}\right)^{k-2} \mathrm{e}^{-\lambda\phi} & r < r_o, \\ -(k^2 + \lambda^2) r_o^{-2} \left(\dfrac{r_o}{r}\right)^{k+2} \mathrm{e}^{-\lambda\phi} & r > r_o, \end{cases} \tag{16}$$

with the cylindrical coordinates (r, ϕ) shown in Fig. 6(a), the solution to (2) is given by

$$T(r, \phi) = \begin{cases} \left(\dfrac{r}{r_o}\right)^k \mathrm{e}^{-\lambda\phi} & r \le r_o, \\ \left(\dfrac{r_o}{r}\right)^k \mathrm{e}^{-\lambda\phi} & r > r_o, \end{cases} \tag{17}$$

where $\lambda = \frac{2k}{\alpha}$. The solution is thus described by the two parameters k and α. As apparent in Fig. 6(b), the temperature gradient is discontinuous across the microchannel but is continuous along the microchannel. The temperature decays slowly in the counter-clockwise direction due to the relatively small value of λ.

Some of the structured non-conforming meshes and the unstructured conforming meshes used in this study are shown in Fig. 7. Unstructured non-conforming meshes have also been used for the NURBS-based IGFEM. By setting

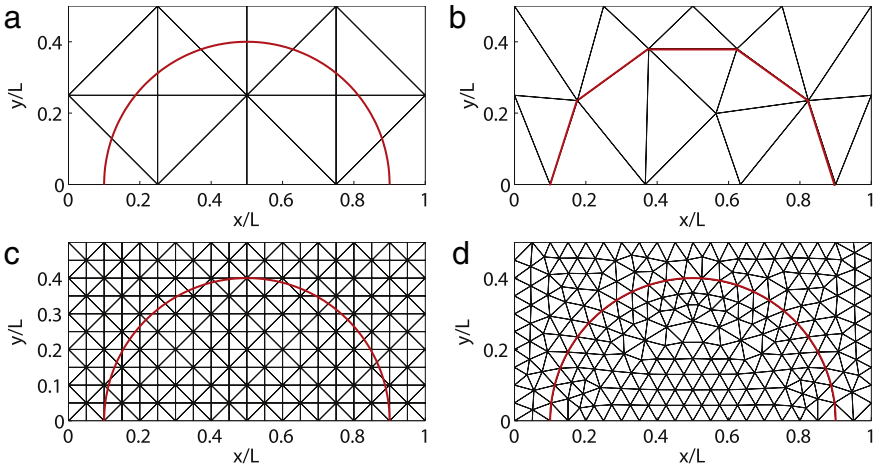

Fig. 7. Non-conforming and conforming meshes for Verification Problem 1. (a) and (b): Coarsest non-conforming and conforming meshes. (c) and (d): Finer non-conforming and conforming meshes.

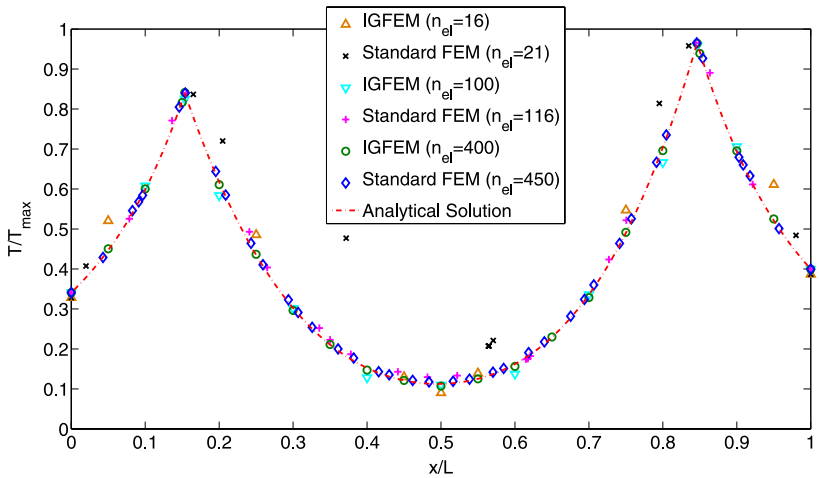

Fig. 8. Comparison of IGFEM and SFEM solutions with analytical solution along the line $y = 0.2L$ (dashed line in Fig. 6(a)) for different number of elements n_{el}.

$k = 3$ and $\alpha = 90$, the solutions obtained from the two coarsest structured non-conforming mesh are compared with those obtained from the two coarsest conforming mesh along the line $y = 0.2L$ in Fig. 8. It can be seen that IGFEM is able to capture the two weak discontinuities at $x = 0.15L$ and $0.85L$ with a relatively coarse mesh and that no significant difference between IGFEM and SFEM is observed as the mesh becomes finer.

The errors in the L^2- and H^1-norms for both IGFEM and SFEM with respect to the minimum edge length for structured meshes or average edge length for unstructured meshes h are compared in Figs. 9(a), (c). As alluded to in Fig. 8, the solution obtained by IGFEM is significantly more accurate for coarse meshes. By fitting the model $\|T - T^h\| = Ah^\beta$ to the last 4 data points, the asymptotic convergence rates of IGFEM with unstructured mesh in the L^2 norm and H^1 norm are 1.95 and 0.93, respectively. With structured mesh, the convergence rates are 1.85 and 0.94 respectively. If the last two data points were used, the convergence rates are 1.93 and 0.96, respectively. The slightly lower accuracy of the structured mesh is due to the higher percentage of very slender integration subdomains, which causes problem in the derivative of the temperature. Note that this problem also occurs in GFEM/XFEM [12,36]. Unlike conventional GFEM for sharp thermal gradient [4], the accuracy of IGFEM is essentially independent of the mesh orientation. On the other hand, the convergence rates of SFEM are 2.09 and 1 respectively. Due to the slightly higher convergence rate of SFEM, its accuracy will eventually become better than IGFEM as the mesh becomes finer.

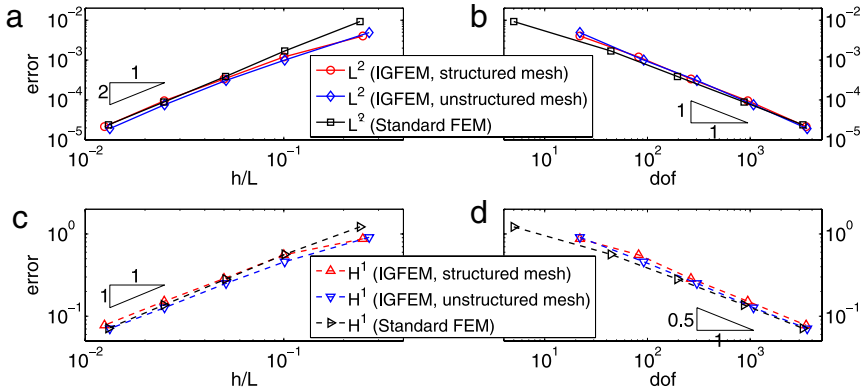

Fig. 9. Convergence study: L^2 (top) and H^1 (bottom) errors for Verification Problem 1 (with $r_o = 0.4L$, $k = 3$ and $\alpha = 90$).

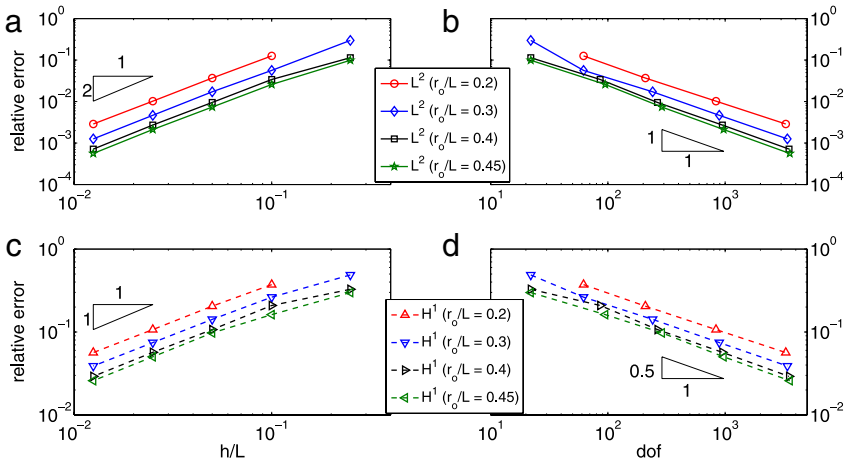

Fig. 10. Effect of curvature on the L^2 and H^1 relative errors for Verification Problem 1 with semicircular channels of different radii, $k = 3$ and $\alpha = 90$.

The mesh size at which this happens, h_o will become smaller as the microchannel effect becomes more important, i.e., as α and/or k increase.

A comparison of the error of IGFEM and that of SFEM with respect to the number of degrees of freedom (total number of nodes less the prescribed nodes) is also shown in Figs. 9(b), (d). The accuracies of both methods are comparable to each other for a given number of dofs, with the slightly higher convergence rate of IGFEM due to the strategic placement of the dofs near the microchannel. However, SFEM has a slightly better accuracy compared to IGFEM for a given dof due to the greater number of elements near the channel and the fact that the total error does not just come from elements cut by the channel but also elements near the channel.

The effect of curvature on the relative error of the solution ($\|T - T^h\|/\|T\|$) is also investigated using IGFEM with a structured mesh by changing the radius of the semicircular channel. Fig. 10 shows that the relative error increases with curvature $1/r_o$ but the convergence rate is essentially unchanged as expected.

4.2. Verification Problem 2: straight channels with branching

Consider the network of branched straight channels in a square domain of length L illustrated in Fig. 11(a). The junction is located at $x_o = y_o = L/2$. A flow $\dot{m}_1$ enters the domain from point $(x_o, 0)$ and splits into 3 microchannels with flow rates $\dot{m}_2, \dot{m}_3, \dot{m}_4$ such that $\dot{m}_1 = \dot{m}_2 + \dot{m}_3 + \dot{m}_4$. Let the dimensionless parameters defined in (15) be $\alpha_i = \dot{m}_i c_f/\kappa$ for channels $i = 1, 2, 3, 4$.

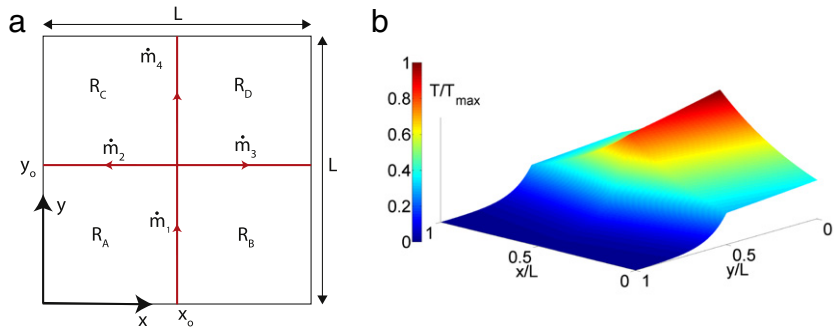

Fig. 11. (a) Domain geometry of Verification Problem 2. (b) 3D surface plot of the analytical temperature field. The temperature is normalized by the maximum temperature in the domain, $T_{\max}$.

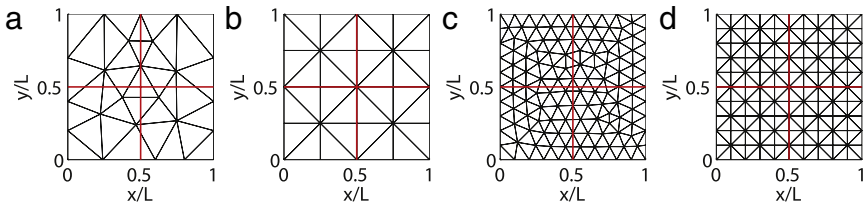

Fig. 12. Non-conforming and conforming meshes for Verification Problem 2. (a) and (b): Coarsest non-conforming and conforming meshes. (c) and (d): Finer non-conforming and conforming meshes.

For the following distributed heat sources:

$$f(x,y) = \begin{cases} -C(\lambda_1^2+\lambda_2^2)e^{\lambda_2 x-\lambda_1 y} & \text{on } R_A, \\ -C(\lambda_1^2+\lambda_3^2)e^{\lambda_2 x_o+\lambda_3(x_o-x)-\lambda_1 y} & \text{on } R_B, \\ -C(\lambda_2^2+\lambda_4^2)e^{\lambda_2 x+\lambda_4(y_o-y)-\lambda_1 y_o} & \text{on } R_C, \\ -C(\lambda_3^2+\lambda_4^2)e^{\lambda_2 x_o+\lambda_3(x_o-x)+\lambda_4(y_o-y)-\lambda_1 y_o} & \text{on } R_D, \end{cases} \tag{18}$$

where the subdomains R_A, R_B, R_C and R_D are shown in Fig. 11(a), the solution to (2) with the appropriate Dirichlet boundary conditions is given by

$$T(x,y) = \begin{cases} Ce^{\lambda_2 x-\lambda_1 y} & \text{on } R_A, \\ Ce^{\lambda_2 x_o+\lambda_3(x_o-x)-\lambda_1 y} & \text{on } R_B, \\ Ce^{\lambda_2 x+\lambda_4(y_o-y)-\lambda_1 y_o} & \text{on } R_C, \\ Ce^{\lambda_2 x_o+\lambda_3(x_o-x)+\lambda_4(y_o-y)-\lambda_1 y_o} & \text{on } R_D, \end{cases} \tag{19}$$

provided the following relations are satisfied: $\lambda_1\alpha_1 = \lambda_4\alpha_4 = \lambda_2+\lambda_3$, $\lambda_2\alpha_2 = \lambda_3\alpha_3 = \lambda_4-\lambda_1$, $\alpha_1 = \alpha_2+\alpha_3+\alpha_4$. The problem is thus defined by 3 parameters, for which we choose $\alpha_1 = 10$, $\alpha_4 = 0.4$ and $\lambda_2 = 20$. Hence $\lambda_1 = 4$, $\lambda_3 = 20$, $\lambda_4 = 100$, $\alpha_2 = \alpha_3 = 4.8$. Fig. 11(b) shows the exact temperature field. Steep jumps in thermal gradient are observed along channels $i = 2, 3, 4$.

We use NURBS with different number of control points n and degree p to describe the straight channels as shown in Table A.2 given in the Appendix. The purpose of doing this is to verify that our method works even for different degree NURBS. Note that the degree of the NURBS enrichment is given by the degree of NURBS curve used to describe the geometry of the microchannel. In general, a lower degree NURBS curve can be integrated more accurately with a given Gaussian quadrature scheme.

Some of the non-conforming and conforming meshes used in this problem are shown in Fig. 12. The solutions obtained with IGFEM with $n = 2$, $p = 1$ and SFEM are compared in Fig. 13, showing that IGFEM achieves a significantly more accurate solution for very coarse meshes.

The error of the IGFEM solution with different n and p is compared with that of SFEM in Figs. 14(a), (c). In spite of the suboptimal convergence rate for large element size h, IGFEM is significantly more accurate than SFEM for

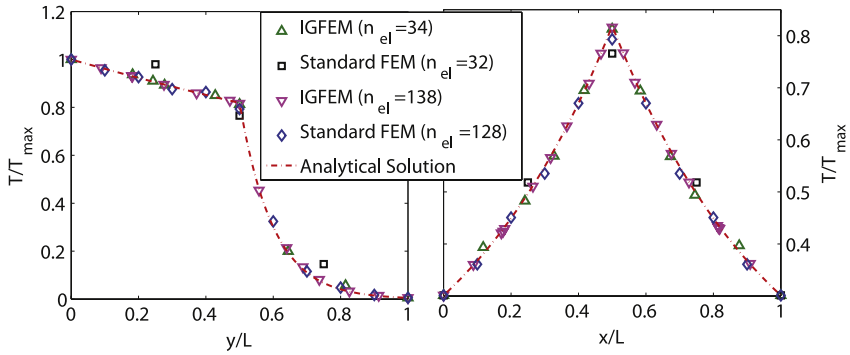

Fig. 13. Comparison of IGFEM and SFEM solutions along the microchannels $x = 0.5L$ (left) and $y = 0.5L$ (right) in Fig. 11(a) for different number of elements n_{el}.

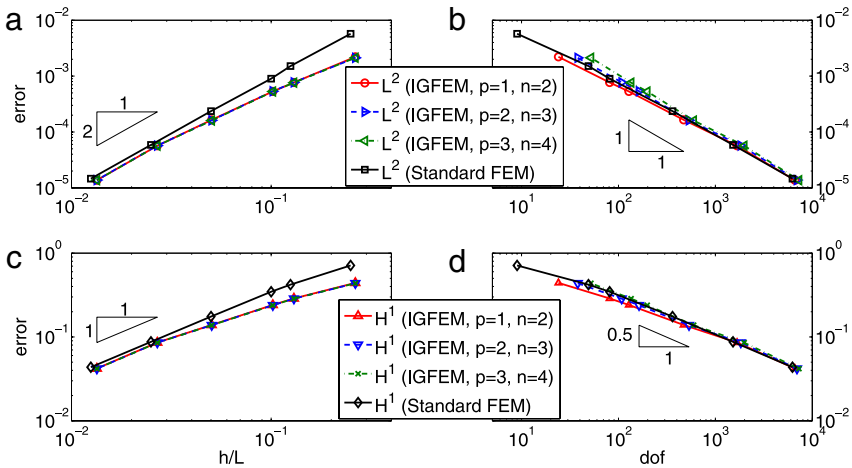

Fig. 14. Convergence analysis: L^2 and H^1 errors for Verification Problem 2. Effect of the degree of NURBS, p, and the number of control points of each microchannel, n, on the L^2 and H^1 errors.

moderate to large h. The asymptotic convergence rates of IGFEM with respect to h in the L^2 and H^1 norms using the last two points are 2.04 and 1.03, respectively, regardless of n and p. This result shows that the NURBS-based IGFEM is able to handle NURBS curves of different degrees.

For a given number of dofs, the IGFEM with $n = 2$, $p = 1$ has slightly better accuracy than the SFEM. However, for straight channels, using a higher number of enrichment nodes or degree of enrichment functions does not improve the accuracy and incurs greater computational cost.

5. Applications

As indicated in the Introduction, recent advances in the manufacturing of microvascular materials allow for very complex curved microchannels to be embedded in polymeric and composite components [1,18]. In the examples presented hereafter, we show that IGFEM is capable of handling many types of complex microchannel configurations.

5.1. Application 1: wavy channel in active cooling of microvascular materials

Inspired by the microchannel design study summarized in [37], we apply the NURBS-based IGFEM to a $L \times L/2$ domain with a curved microchannel as shown in Fig. 15(a). The microchannel is described by a degree-2 NURBS with the control points (0, 0.3), (0.2, 0.045), (0.4, 0.455), (0.6, 0.045), (0.8, 0.455), (1, 0.2) and knot vector $\{0, 0, 0, 1, 2, 3, 4, 4, 4\}$. Note that the coordinates of the control points are expressed in terms of the characteristic

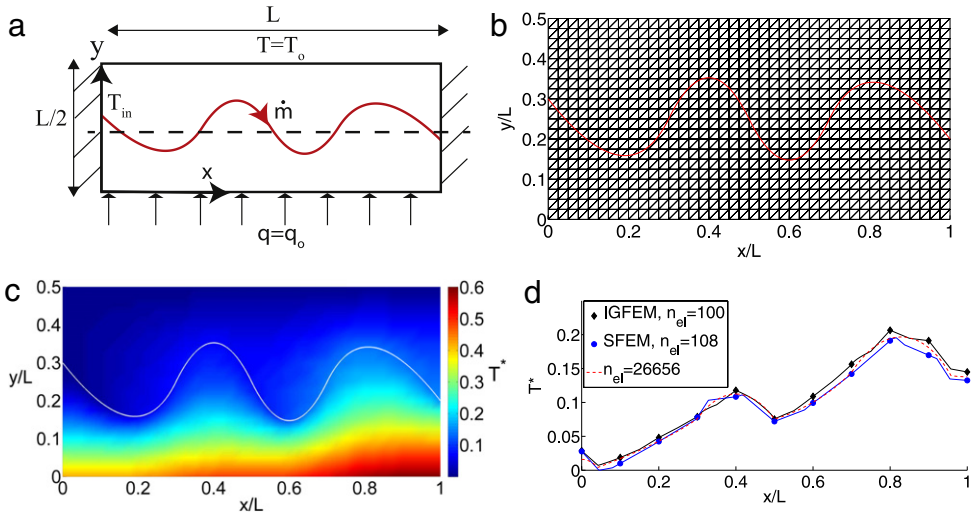

Fig. 15. (a) Domain geometry and boundary conditions for Application Problem 1. (b) Non-conforming mesh used by IGFEM to produce the temperature field in (c). (d) Temperature along the line $y = 0.25L$ (dashed line in (a)). The parameters are $\alpha = \dot{m}c_f/\kappa = 10$ and $T_{\text{in}} = T_o$.

length L and all weights associated with the control points are unity. A heat flux q_o is applied along the bottom edge of the domain and the temperature is fixed ($T = T_o$) along the top edge. The temperature at the inlet of the channel, T_{in} is prescribed. The solution is expressed in terms of the dimensionless temperature

$$T^* = \frac{2\kappa}{q_o L}(T - T_o), \tag{20}$$

where $\frac{q_o L}{2\kappa} + T_o$ is the maximum temperature in the absence of the microchannel. The temperature distribution in Fig. 15(c) obtained using the mesh in Fig. 15(b) shows that fluid flow in the microchannel reduces the maximum temperature relative to that without the microchannel.

The IGFEM solutions are compared with SFEM solutions obtained with coarser conforming meshes of the same sizes as the structured meshes and a very fine conforming mesh in Fig. 15(d) along the line $y = 0.25L$. Both IGFEM and SFEM are able to obtain the solution with rather coarse meshes. The reference maximum temperature is 0.604. For IGFEM, the predicted maximum temperature with 100 elements has a relative error of 1.3% compared to 3.14% for SFEM with 108 elements and the same mesh size.

5.2. Application 2: serpentine microchannel

Motivated by the use of serpentine channels employed in battery cooling plates [38], we use the IGFEM thermal solver to analyze the temperature distribution in a thin microvascular domain represented by a square domain of length L with a serpentine microchannel as shown in Fig. 16(a) with different flow rates, $\dot{m}_f = \dot{m}, 2\dot{m}, 4\dot{m}$. The microchannel is represented by a single quadratic NURBS curve with control points (0, 0.1), (0.89, 0.039), (0.89, 0.69), (0.3, 0.69), (0.3, 0.5), (0.7, 0.6), (0.6, 0.25), (0.19, 0.25), (0.19, 0.98), (1, 0.9) and knot vector {0, 0, 0, 1, 2, 3, 4, 5, 6, 7, 8, 8, 8}. As before, the weights associated with the control points are unity. All sides of Ω are insulated except at one point where the temperature of the microchannel at the inlet, T_{in} is prescribed. The heat flux on the flat face of Ω is modeled as a uniform distributed source, i.e., $f(x, y) = Q_b$ in (2). The solution is expressed in terms of a dimensionless temperature defined by

$$T^* = \frac{T - T_{\text{in}}}{T_c}, \tag{21}$$

where the characteristic temperature is defined as $T_c = Q_b L^2/\kappa$. Hence, the dimensionless distributed heat source, $Q_b L^2/\kappa T_c$ is 1. The effect of increasing the flow rate is clearly seen in Figs. 16(b)–(d).

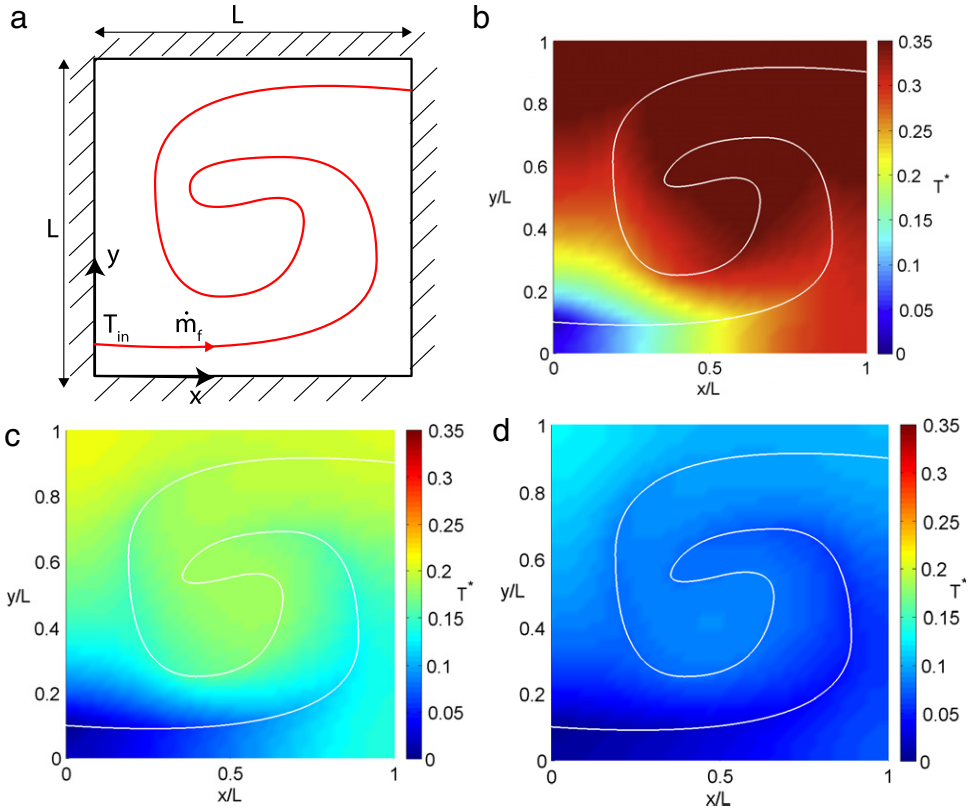

Fig. 16. (a) Domain geometry and boundary conditions of a material with a serpentine microchannel and uniform body source, Q_b. The temperature fields obtained using a structured mesh with 3200 elements for (b) $\dot{m}_f = \dot{m}$, $\alpha = 2.5$, (c) $\dot{m}_f = 2\dot{m}$, $\alpha = 5$ and (d) $\dot{m}_f = 4\dot{m}$, $\alpha = 10$, where $\alpha = \dot{m}_f c_f/\kappa$.

5.3. Application 3: embedded network of wavy channels

The design optimization of the microchannels in a microvascular material to minimize objective functions such as global flow resistance, void volume fraction and maximum temperature has been a subject of a number of studies [5,6,37,39]. One notable result is that to minimize the global flow resistance, it is more efficient to bathe a region with a single stream of microchannels with branching than multiple streams of microchannels [39]. In this final application, we replace the single microchannel in Fig. 15(a) with a network of microchannels as shown in Fig. 17(a). The knot vectors and the control points are shown in Table A.3 given in the Appendix. A single stream of mass flow rate $\dot{m}$ is split into four microchannels each having the same mass flow rate of $\dot{m}/4$. The solution is expressed in terms of the dimensionless temperature defined in (20). The temperature distribution in Fig. 17(c) obtained using the non-conforming mesh in Fig. 17(b) clearly shows the cooling effect of the microchannels.

A comparison of the IGFEM and SFEM solutions along the line $y = 0.25L$ in Fig. 17(d) shows that both methods with relatively coarse meshes agree with the reference solution obtained with a fine conforming mesh. A closer look at the spike at around $x = 0.9L$ close to a branching point shows that IGFEM is able to model the spike more accurately than SFEM. Using the maximum temperature of 0.597 provided by the reference solution as the reference, the error of the maximum temperature predicted by IGFEM with 400 elements is 0.088%, compared to 2.3% predicted by SFEM with 452 elements.

6. Conclusions

The formulation and implementation of a NURBS-based IGFEM have been presented for the thermal analysis of a material containing curved microchannels based on a simplified model of the cooling or heating effect of the embedded network. The method is capable of preserving the exact geometrical description of the curved microchannels.

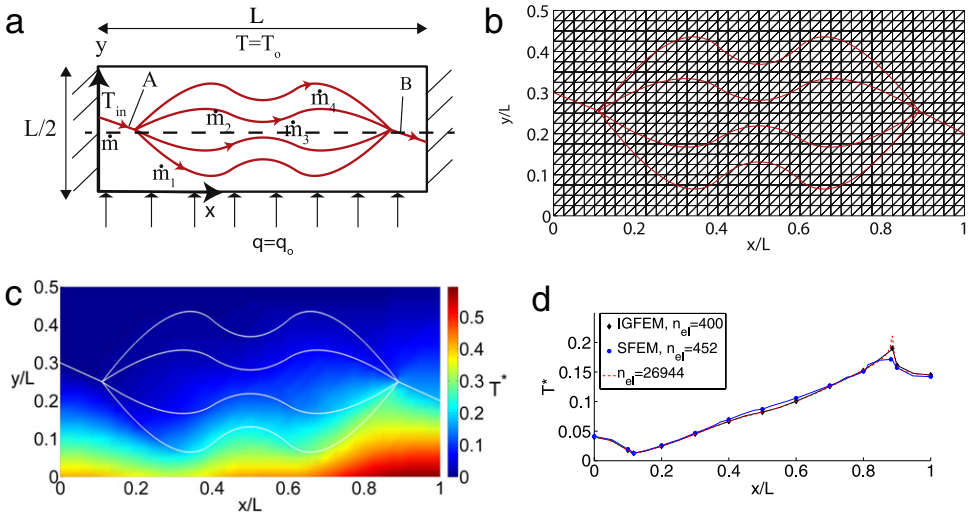

Fig. 17. (a) Domain geometry and boundary conditions for Application Problem 3. (b) Non-conforming mesh used by IGFEM solver to obtain the temperature field shown in (c). (d) The temperature along the line $y = 0.25L$ (dashed line in (a)). The parameters are $\alpha = \dot{m}c_f/\kappa = 10$, $\dot{m}_i = \dot{m}/4$, $(i = 1, 2, 3, 4)$, $T_{\text{in}} = T_o$.

Table A.1
Knot vectors and control points for the numerical integration study in Section 3.5. The last two NURBS curves are circular arcs of radii 1.6 and 8, respectively.

n	p	Knot vector	Control points	Weights
4	2	{0, 0, 0, 0.5, 1, 1, 1}	(0, 0), (0.3, 0.25), (0.7, 0.05), (1.0, 0.0)	1, 1, 1, 1
5	3	{0, 0, 0, 0, 0.5, 1, 1, 1, 1}	(0, 0), (0.2, 0.2), (0.5, 0.05), (0.8, 0.15), (1.0, 0.0)	1, 1, 1, 1, 1
3	2	{0, 0, 0, 1, 1, 1}	(0, 0), (0.5, 0.1645), (1, 0)	1, 0.950, 1
3	2	{0, 0, 0, 1, 1, 1}	(0, 0), (0.5, 0.03131), (1, 0)	1, 0.998, 1

Table A.2
Knot vectors and control points for Verification Problem 2. The microchannels are described by different degree NURBS, p and different number of control points, n. The coordinates are expressed in terms of the characteristic length L. All weights are unity.

n	p	Knot vector	Channel	Control points
2	1	{0, 0, 1, 1}	1	(0.50, 0), (0.50, 0.50)
			2	(0.50, 0.50), (0, 0.50)
			3	(0.50, 0.50), (1, 0.50)
			4	(0.50, 0.50), (0.50, 1)
3	2	{0, 0, 0, 1, 1, 1}	1	(0.50, 0), (0.50, 0.25), (0.50, 0.50)
			2	(0.50, 0.50), (0.25, 0.50), (0, 0.50)
			3	(0.50, 0.50), (0.75, 0.50), (1, 0.50)
			4	(0.50, 0.50), (0.50, 0.75), (0.50, 1)
4	3	{0, 0, 0, 0, 1, 1, 1, 1}	1	(0.50, 0), (0.50, 0.15), (0.50, 0.35), (0.50, 0.50)
			2	(0.50, 0.50), (0.35, 0.50), (0.15, 0.50), (0, 0.50)
			3	(0.50, 0.50), (0.65, 0.50), (0.85, 0.50), (1, 0.50)
			4	(0.50, 0.50), (0.50, 0.65), (0.50, 0.85), (0.50, 1)

It is also able to handle branching in the interior of an element. The enrichment functions are simply constructed from some of the basis functions of the NURBS description of the integration subdomains. It has been shown that NURBS-based IGFEM obtains close-to-optimal rate of convergence even for curved microchannel and is more accurate than SFEM for coarse meshes. The method was then applied to solve a number of problems with complex

Table A.3
Knot vectors and control points for Application Problem 3 expressed in terms of the characteristic length L. All weights are unity.

Channel	Knot vector	Control points
A	{0, 0, 1, 1}	(0, 0.300), (0.110, 0.255)
B	{0, 0, 1, 1}	(0.890, 0.255), (1, 0.200)
1	{0, 0, 0, 1, 2, 3, 3, 3}	(0.110, 0.255), (0.300, 0.500), (0.500, 0.325), (0.700, 0.500), (0.890, 0.255)
2	{0, 0, 0, 1, 2, 3, 3, 3}	(0.110, 0.255), (0.300, 0.375), (0.500, 0.250), (0.700, 0.375), (0.890, 0.255)
3	{0, 0, 0, 1, 2, 3, 3, 3}	(0.110, 0.255), (0.300, 0.125), (0.500, 0.250), (0.700, 0.125), (0.890, 0.255)
4	{0, 0, 0, 1, 2, 3, 3, 3}	(0.110, 0.255), (0.300, 0), (0.500, 0.175), (0.700, 0), (0.890, 0.255)

microchannel configurations. The ability of the method to provide a good approximation of the thermal field for complex microchannel networks with a relatively coarse non-conforming mesh is expected to be especially attractive in its 3D implementation currently under development.

Acknowledgments

The authors wish to thank Stephen J. Pety for bringing their attention to the serpentine channel configuration in battery cooling plates. This work has been supported by the Air Force Office of Scientific Research Multidisciplinary University Research Initiative (Grant No. FA9550-09-1-0686), with David Stargel as Program Director.

Appendix

See Tables A.1–A.3.

References

[1] A.P. Esser-Kahn, P.R. Thakre, H. Dong, J.F. Patrick, V.K. Vlasko-Vlasov, N.R. Sottos, J.S. Moore, S.R. White, Three-dimensional microvascular fiber-reinforced composites, Adv. Mater. 23 (2011) 3654–3658.
[2] D. Therriault, S.R. White, J.A. Lewis, Chaotic mixing in three-dimensional microvascular networks fabricated by direct-write assemble, Nature Mater. 2 (2003) 265–271.
[3] K.S. Toohey, N.R. Sottos, J.A. Lewis, J.S. Moore, S.R. White, Self-healing materials with microvascular networks, Nature Mater. 6 (2007) 581–585.
[4] P. O'Hara, C.A. Duarte, T. Eason, Generalized finite element analysis of three-dimensional heat transfer problems exhibiting sharp thermal gradients, Comput. Methods Appl. Mech. Engrg. 198 (2009) 1857–1871.
[5] A.M. Aragón, K.J. Smith, P.H. Geubelle, S.R. White, Multi-physics design of microvascular materials for active cooling applications, J. Comput. Phys. 230 (2011) 5178–5198.
[6] A.M. Aragón, R. Saksena, B.D. Kozola, P.H. Geubelle, K.T. Christensen, S.R. White, Multi-physics optimization of three-dimensional microvascular polymeric components, J. Comput. Phys. 233 (2013) 132–147.
[7] A. Combescure, A. Gravouil, D. Grégoire, J. Réthoré, X-FEM a good candidate for energy conservation in simulation of brittle dynamic crack propagation, Comput. Methods Appl. Mech. Engrg. 197 (2008) 309–318.
[8] C.A. Duarte, I. Babuška, J.T. Oden, Generalized finite element method for three-dimensional structural mechanics problems, Comput. Struct. 77 (2000) 215–232.
[9] C. Daux, N. Moës, J. Dolbow, N. Sukumar, T. Belytschko, Arbitrary branched and intersecting cracks with the extended finite element method, Internat. J. Numer. Methods Engrg. 48 (2000) 1741–1760.
[10] J.M. Melenk, I. Babuška, The partition of unity finite element method: basic theory and applications, Comput. Methods Appl. Mech. Engrg. 139 (1996) 289–314.
[11] I. Babuška, J.M. Melenk, The partition of unity method, Internat. J. Numer. Methods Engrg. 40 (1997) 727–758.
[12] T.-P. Fries, T. Belytschko, The extended/generalized finite element method: an overview of the method and its applications, Internat. J. Numer. Methods Engrg. 84 (2010) 253–304.
[13] C.A. Duarte, L. Reno, A. Simone, A high-order generalized FEM for through-the-thickness branched cracks, Internat. J. Numer. Methods Engrg. 72 (2007) 325–351.
[14] N. Moës, M. Cloirec, P. Cartraud, J.-F. Remacle, A computational approach to handle complex microstructure geometries, Comput. Methods Appl. Mech. Engrg. 192 (2003) 3163–3177.
[15] A.M. Aragón, C.A. Duarte, P.H. Geubelle, Generalized finite element enrichment functions for discontinuous gradient fields, Internat. J. Numer. Methods Engrg. 82 (2009) 242–268.
[16] S. Soghrati, A.M. Aragón, C.A. Duarte, P.H. Geubelle, An interface-enriched generalized FEM for problems with discontinuous gradient fields, Internat. J. Numer. Methods Engrg. 89 (2012) 991–1008.

[17] S. Soghrati, P.H. Geubelle, A 3D interface-enriched generalized finite element method for weakly discontinuous problems with complex internal geometries, Comput. Methods Appl. Mech. Engrg. 217–220 (2012) 46–57.
[18] S.C. Olugebefola, A.M. Aragón, C.J. Hansen, A.R. Hamilton, B. Kozola, W. Wu, P.H. Geubelle, J.A. Lewis, N.R. Sottos, S.R. White, Polymer microvascular network composites, J. Compos. Mater. 44 (2010) 2587–2603.
[19] K.W. Cheng, T.-P. Fries, Higher-order XFEM for curved strong and weak discontinuities, Internat. J. Numer. Methods Engrg. 82 (2010) 564–590.
[20] D.F. Rogers, An Introduction to NURBS with Historical Perspective, Morgan Kaufmann Publishers, 2011.
[21] L. Piegl, W. Tiller, The NURBS Book, Springer, 1997.
[22] T.J.R. Hughes, J.A. Cottrell, Y. Bazilevs, Isogeometric analysis: CAD, finite element, NURBS, exact geometry and mesh refinement, Internat. J. Numer. Methods Engrg. 194 (2005) 4135–4195.
[23] J.A. Cottrell, T.J.R. Hughes, Y. Bazilevs, Isogeometric Analysis: Toward Integration of CAD and FEA, John Wiley and Sons, 2009.
[24] R. Sevilla, S. Fernández-Méndez, A. Huerta, NURBS-enhanced finite element method (NEFEM), Arch. Comput. Methods Eng. 18 (2011) 441–484.
[25] G. Haasemann, M. Kästner, S. Prüger, V. Ulbricht, Development of a quadratic finite element formulation based on the XFEM and NURBS, Internat. J. Numer. Methods Engrg. 86 (2011) 598–617.
[26] G. Legrain, A NURBS enhanced extended finite element approach for unfitted CAD analysis, Comput. Mech. 59 (2013) 913–929.
[27] W.M. Kays, M.E. Crawford, Convective Heat and Mass Transfer, McGraw-Hill, 1993.
[28] A.N. Brooks, T.J.R. Hughes, Streamline upwind/Petrov–Galerkin formulations for convection dominated flow with particular emphasis on the incompressible Navier–Stokes equation, Comput. Methods Appl. Mech. Engrg. 32 (1982) 199–259.
[29] W.G. Habashi, J. Dompierre, Y. Bourgault, D. Ait-Ali-Yahia, M. Fortin, M.-G. Vallet, Anisotropic mesh adaptation: towards user-independent, mesh-independent and solver-independent CFD. Part I: general principles, Internat. J. Numer. Methods Fluids 32 (2000) 725–744.
[30] D.W. Marquardt, An algorithm for least-squares estimation of nonlinear parameters, J. Soc. Ind. Appl. Math. 11 (1963) 431–441.
[31] T.J.R. Hughes, A. Reali, G. Sangalli, Efficient quadrature for NURBS-based isogeometric analysis, Comput. Methods Appl. Mech. Engrg. 199 (2010) 301–313.
[32] J.M. Lane, R.F. Riesenfeld, A theoretical development for the computer generation and display of piecewise polynomial surfaces, IEEE Trans. Pattern Anal. Mach. Intell. 2 (1980) 35–46.
[33] P.A. Koparkar, S.P. Mudur, A new class of algorithms for the processing of parametric curves, Comput.-Aided Des. 15 (1983) 41–45.
[34] T.W. Sederberg, S.R. Parry, Comparison of three curve intersection algorithms, Comput.-Aided Des. 18 (1986) 58–63.
[35] T.W. Sederberg, T. Nishita, Curve intersection using Bézier clipping, Comput.-Aided Des. 22 (1990) 538–549.
[36] L.V. Miegroet, P. Duysinx, Stress concentration minimization of 2D filets using X-FEM and level set description, Struct. Multidiscip. Optim. 33 (2007) 425.
[37] S. Soghrati, P.R. Thakre, S.R. White, N.R. Sottos, P.H. Geubelle, Computational modeling and design of actively-cooled microvascular materials, Int. J. Heat Mass Transfer 55 (2012) 5309–5321.
[38] A. Jarrett, I.Y. Kim, Design optimization of electric vehicle battery cooling plates, J. Power Sources 196 (2011) 10359–10368.
[39] S. Kim, S. Lorente, A. Bejan, Vascularized materials: tree-shaped flow architectures matched canopy to canopy, J. Appl. Phys. 100 (2006) 063525.